Relations between geological characteristics and satellite-derived infrared and microwave emissivities over deserts in northern Africa and the Arabian Peninsula

Carlos Jiménez, Julie Catherinot, Catherine Prigent, Jack Roger

Relations between geological characteristics and satellite-derived infrared and microwave emissivities over deserts in northern Africa and the Arabian Peninsula

Carlos Jiménez,[1] Julie Catherinot,[1] Catherine Prigent,[1] and Jack Roger[2]

Received 27 January 2010; revised 4 May 2010; accepted 12 July 2010; published 30 October 2010.

[1] Infrared and microwave emissivities have been previously calculated over the globe from satellite observations to estimate the longwave radiative budget of the planet in global circulation models (GCM) or to facilitate the assimilation of surface-sensitive satellite observations over land in numerical weather prediction (NWP) models. This study examines the relationship between these emissivities and the soil lithology over the deserts in northern Africa and the Arabian Peninsula at large scales. For this purpose, a lithology map of the area has been carefully derived from combining several geological maps and in situ lithostratigraphic columns. Infrared and microwave emissivities show large spatial variability, much more than often assumed in GCM or in NWP models, that relate well to the surface properties, especially the lithology. Changes in the lithology explain ~40% and up to 50% of the emissivities variability at the considered frequencies in the infrared and in the microwaves. In particular, siliceous and carbonate outcrops have specific signatures that can be identify in these wavelength ranges, with a surprisingly good sensitivity of the microwaves to the presence of carbonates. This study clearly indicates that geological information is necessary for emissivity modeling, not only in the infrared but also in the microwaves, for GCM and NWP applications. The lithology maps created from the geological maps for this study is available under request. Our study also suggests that the combination of infrared and microwave emissivities has some potential for lithology mapping at large scales, especially for land surface models.

Citation: Jiménez, C., J. Catherinot, C. Prigent, and J. Roger (2010), Relations between geological characteristics and satellite-derived infrared and microwave emissivities over deserts in northern Africa and the Arabian Peninsula, *J. Geophys. Res.*, *115*, D20311, doi:10.1029/2010JD013959.

1. Introduction

[2] Land surface emissivity in atmospheric windows is an important parameter, first, for the estimation of the Earth radiation budget and, second, to derive atmospheric information from surface-sensitive satellite observations.

[3] First, infrared surface emissivity e_{IR} plays a direct key role in the radiation budget, with the long wave surface radiation proportional to $e_{IR}T_S^4$, where T_S is the surface skin temperature. Indirectly as well, infrared emissivity intervenes in the satellite estimation of T_S that can then be used to estimate the longwave surface radiation. Under cloudy conditions, infrared measurements from satellites cannot provide T_S estimates and methods are developed to derive this information from microwaves, with the microwave signal proportional to $e_{IR}T_S$ in atmospheric windows at first order [e.g., *Aires et al.*, 2001].

[4] Second, in numerical weather prediction (NWP) schemes, assimilation of surface-sensitive satellite observations for the estimation of the lower atmosphere requires an estimate of the surface emissivity. For both infrared and microwave sounding observations that are sensitive to the surface, the surface contribution has to be evaluated and subtracted in order to extract the atmospheric information [e.g., *Weng and Liu*, 2003; *Prigent et al.*, 2005a].

[5] Nevertheless, land surface emissivities are often crudely estimated in land surface models, in general circulation models (GCMs), or in assimilation schemes, with fixed emissivities for a given surface type or even fixed emissivity regardless of surface type. For instance, the infrared land surface emissivity is prescribed to a value of 1 in the GCMs of the Center for Ocean-Land-Atmosphere Studies (COLA) [*Kinter et al.*, 1988] and a fixed soil emissivity of 0.96 is used in the Common Land Model (CLM0) [*Zeng et al.*, 2002; *Dai et al.*, 2003].

[6] Maps of land surface emissivities at the continental scale have been estimated from satellite observations and are now available to the community, both in the infrared [e.g., *Wan and Li*, 1997; *Seemann et al.*, 2008; *Li et al.*, 2007; *Hulley and Hook*, 2009] and in the microwaves [e.g., *Prigent*

[1]Laboratoire d'Etudes du Rayonnement et de la Matière en Astrophysique, CNRS, Observatoire de Paris, Paris, France.
[2]Bureau des Ressources Géologiques et Minières, Orléans, France.

0148-0227/10/2010JD013959

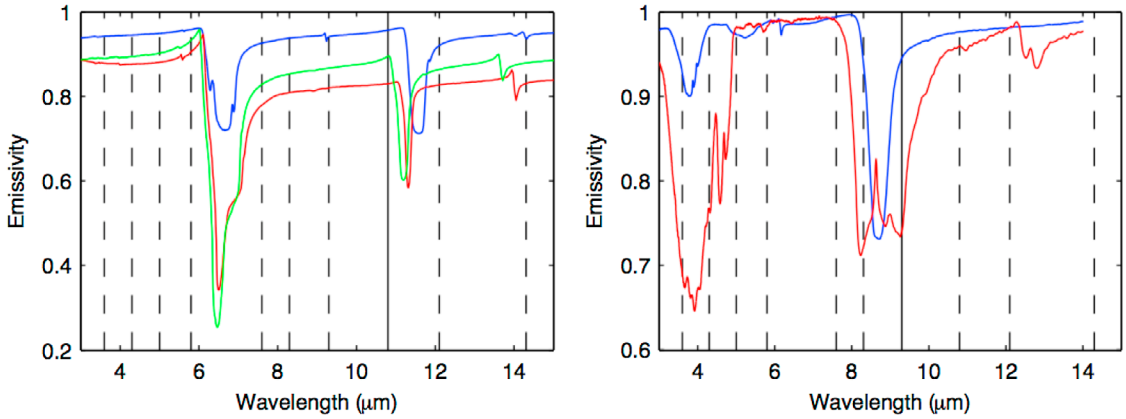

Figure 1. Examples of measured infrared emissivities for different mineral and soil types. The left plot shows the spectral signatures for three carbonate minerals: aragonite (blue), dolomite (green), and calcite (red). The right plot shows the signatures for two soils composed of silicate minerals: a sand dune with white gypsum (blue) and alluvial sands rich in quartz (red). The vertical lines mark the channels of the *Seemann et al.* [2008] data set (solid for the channels selected here for carbonate and silicate analysis, dashed for the remaining channels). The measurements are reproduced from the ASTER Spectral Library [*Baldridge et al.*, 2009] through the courtesy of the Jet Propulsion Laboratory, California Institute of Technology, Pasadena, California.

et al., 1997, 2006; *Karbou et al.*, 2005]. They show much more spatial variability than prescribed in the GCM or NWP models, especially over arid and semiarid regions. Pioneering work by *Allison* [1977] already showed spatial patterns in the microwave measured radiances in the Middle East related to geological structures. More recently, a few studies over deserts already showed large variability at regional scales, both in the infrared [*Zhou et al.*, 2003; *Ogawa et al.*, 2003] and in the microwaves [*Prigent et al.*, 2005b].

[7] In this study, we propose a joint analysis of satellite-derived emissivities in the infrared and microwaves over Northern Africa and the Arabian Peninsula in order to better understand the relation between the emissivities and the surface lithology and to check the consistency of the two emissivity data sets with respect to the surface properties. Longer term goals are to evaluate the potential of each wavelength range for geological characterization and to provide alternatives to better specify the emissivities in GCMs and in NWP schemes.

[8] Two global reference emissivity data sets are adopted: the *Seemann et al.* [2008] database in the infrared and the *Prigent et al.* [2006] in the microwaves. The emissivity data sets are first described, along with the geological information used in this study (section 2). The relation between the emissivity and the lithology is carefully analyzed and a tentative mapping of the lithology from the emissivities is proposed (section 3). Section 4 concludes this study.

2. Description of the Satellite Data and Derivation of the Geological Information

2.1. The Satellite-derived Infrared Emissivities

[9] A global infrared land surface emissivity data set derived from a combination of the satellite derived Moderate Resolution Imaging Spectroradiometer (MODIS) emissivities and laboratory measurements have been adopted for this study [*Seemann et al.*, 2008]. The operational land surface emissivity product (MOD11) [*Wan and Li*, 1997; *Wan*, 2008] has a relatively high spatial resolution (0.05° in the monthly averaged product) but limited spectral resolution (emissivity reported at six wavelengths in three spectral regions in the 3.8 to 12 μm range). Laboratory measurements can provide high spectral resolution, but there are not a true representation of the ecosystems as seen from space. In *Seemann et al.* [2008] the high spectral resolution measurements from the MODIS emissivity library (htpp://www.icess.ucsb.edu/modis/EMIS/html/em.html) and the Advanced Spaceborne Thermal Emission and Reflection Radiometer (ASTER) spectral library [*Salisbury et al.*, 1994; *Baldridge et al.*, 2009] are used to fill in the spectral gaps in the MOD11 product. The resulting product estimates global monthly mean emissivities at 10 different wavelengths (3.6, 4.3, 5.0, 5.8, 7.6, 8.3, 9.3, 10.8, 12.1, and 14.3 μm) for the period 2003–2005. To allow comparison with the microwave emissivities, the original spatial resolution is downgraded to the coarser spatial grid of the microwave emissivities (0.25° × 0.25° equal area grid at the equator).

[10] In the infrared, expected narrowband spectral features related to the chemical composition of the minerals are well reproduced by laboratory measurements. Figure 1 shows examples of measured infrared emissivities associated to different minerals. The absorption features near 7, 11, and 14 μm result from vibrations of the C–O bonds in the carbonate anion. Quartz related features near 4, 8, and 13 μm are attributed to O–Si–O stretching vibrations. These features have also been identified in satellite emissivities and attributed to known surface types in arid regions but only for limited areas [e.g., *Zhou et al.*, 2003]. At larger scales, *Chédin et al.* [2004] identified some signatures of sand and carbonates from emissivity maps over northern Africa derived from the High Resolution Infrared Radiation Sounder (HIRS-2) on board the National Oceanic and Atmosphere Administration (NOAA) polar satellites. A detailed study of the expected spatial variability of the emissivities in relation

with the observed geological structures will be presented here.

2.2. The Satellite-derived Microwave Emissivities

[11] Microwave emissivities of land surfaces have been estimated from the Special Sensor Microwave/Imager (SSM/I) observations, between 19 and 85 GHz, by removing contributions from the atmosphere, clouds, and rain using ancillary data from the International Satellite Cloud Climatology Project (ISCCP) [*Rossow and Schiffer*, 1999] and meteorological reanalysis. Cloud-free SSM/I observations are first isolated using collocated visible/infrared satellite observations (ISCCP data). The cloud-free atmospheric contribution is then calculated from an estimate of the local atmospheric temperature-humidity profile from atmospheric reanalysis. Finally, with the surface skin temperature derived from IR observations (ISCCP estimate), the surface emissivity is calculated for all SSM/I channels. The standard deviation of day-to-day variations of the emissivities retrieved over a month are typically less than 0.02, which is a measure of the precision of these estimates. Monthly mean values are calculated at 19.35, 22.235, 37.0, and 85.5 GHz for both vertical (V) and horizontal (H) polarizations (except at 22 GHz), with a spatial resolution of 0.25° × 0.25° equal area grid at the equator. See *Prigent et al.* [2006] for more details.

[12] In the microwave, specific sensitivity to the lithology is usually not recognized. However, a previous study evidenced the sensitivity of the emissivities to the nature of the outcrops, in Oman and Egypt [*Prigent et al.*, 2005b]. Surprisingly low emissivities showed very good spatial correspondences with the presence of carbonated surfaces. In the microwave, the permittivity is the physical variable that intervenes in the emissivity calculation to account for the interaction of the radiation with the nature of the material. Permittivity measurements of rocks are relatively scarce [*Campbell and Ulrichs*, 1969; *Nelson et al.*, 1989; *Lebron et al.*, 2004; *Thomas*, 2006]. They tend to indicate that the permittivity of rocks increases with their carbonate contents, reaching up to ~9, whereas values of permittivity for granite or siliceous rocks are typically around 5. This translates into a decrease of the emissivity with carbonate contents (see simulations of the emissivities for a range of permittivity and roughness in [*Prigent et al.*, 2005b]). One objective of the present study is to confirm the sensitivity of the microwave emissivities to lithology, at continental scale.

2.3. Lithology Mapping

[13] Both infrared and microwave measurements selected in this study are essentially sensitive to the very top layer of the surface, although some microwave penetration has been observed in sand dunes [*Prigent et al.*, 1999]. As a consequence, a description of the outcrops is necessary to relate to the satellite-derived emissivities. However, classical geological maps essentially provide the age of the geological material but not directly the lithology.

[14] The lithology map in this study is derived from the combination of different information sources. First, geological maps from the United States Geological Survey (USGS) (the 1:2,500 000-scale "Bedrock Geology of the Arabian Peninsula and Selected Adjacent Areas") were downloaded in vectorial form. The maps give the age of the different geological units. For a few of the geological units the rock type is also given (e.g., igneous rocks, such as granite or basalt, and special types, such as sand, evaporite, or ophiolite), but for the majority of the rocks of the study area the rock type is not described. Some of these rocks date from Precambrian times (1000–540 Myr), but the majority are Phanerozoic (540–0 Myr) sedimentary rocks. In order to know the composition of the sedimentary rocks, 20 lithostratigraphic columns established by in situ studies were consulted. These columns give the sedimentary outcrop for a range of geological ages at specific locations and allow us to interpret each vector unit of the USGS geological map in terms of rock type. Note that the same methodology cannot be applied to the Precambian rocks due to their much larger spatial heterogeneity related to their age and to the more complex geological deformations undergone by these rocks.

[15] The lithology information from the columns has to be spatially extrapolated to all our study area. To minimize the uncertainties induced by the extrapolation, the resulting map was compared with the 2003 digital soil maps of the Food and Agriculture Organization (FAO), which give an idea about the chemical composition of the outcrops. The results were further refined by also consulting maps of mining resources and through discussions with geologists with ground experience. To allow the joint analysis with the emissivities, the map was then converted from the original vectorial form (1000 m average spatial resolution) to the 0.25° × 0.25° grid of the emissivities. The final map (see Figure 2) was produced by grouping rocks, first, by their type (sedimentary, igneous, or metamorphic) and, second, by their chemical composition. This is a challenging exercise, given the geological complexity at these scales and the difficulty to associate geological age and lithology. Due to the coarse spatial resolution, a pixel in the map is often a mix of different rocks. In this case, the name of the mix is attributed in order of abundance (see the legend in Figure 2). The Precambrian rocks are labeled as "Precambian shield."

3. Results and Discussion

3.1. Spatial Variability of the Emissivities and Relation with the Lithology

[16] The spatial variability of the emissivities and their relation to the lithology are illustrated here by studying the 9.3 μm, 10.8 μm, and the 37 GHz emissivities for V and H polarizations. From the available emissivities in the data set of *Seemann et al.* [2008], the 9.3 and 10.8 μm channels are selected due to their expected sensitivity to the presence of siliceous and carbonate rocks, as described in section 2.1 and illustrated in Figure 1. In the microwave, narrowband absorption features are not expected and are not visible in the available SSM/I-derived emissivity maps between 19 and 85 GHz (rather similar spatial structures are observed at all frequencies). The choice of the 37 GHz emissivities is motivated by a compromise between spatial resolution (degraded spatial resolution at lower frequency) and potential contamination by atmospheric water vapor and clouds (increased contamination at higher frequencies) [*Prigent et al.*, 1997].

[17] Maps of the 2003 yearly averaged V and H emissivities at 37 GHz, along with the polarization difference (V-H), over northern Africa and the Arabian Peninsula, are presented in Figure 3. The main features are very stable over long time periods (several years of data have been examined).

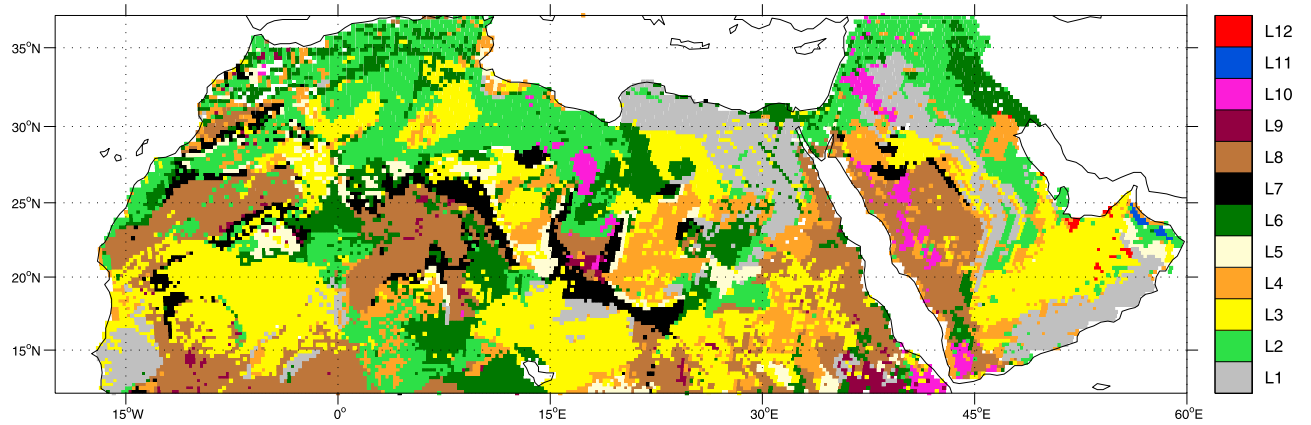

Figure 2. Lithology map of Northern Africa and the Arabian Peninsula derived during the study. The legend corresponds as follows: L1, carbonate rocks; L2, carbonate, siliceous, and evaporite rocks; L3, loose siliceous rocks; L4, indurated siliceous rocks; L5, siliceous, argillaceous, and evaporite rocks; L6, siliceous, argillaceous, and carbonate rocks; L7, siliceous and argillaceous rocks; L8, Precambrian shield; L9, granite; L10, basalt; L11, ophiolite; L12, evaporite.

Low microwave emissivities observed over coastal regions are due to the presence of water in the coastal pixels. Low values can also be observed over the south of the Arabian Peninsula and in northeast Egypt, which have shown correlation with the distribution of outcrops with large proportion of carbonate rocks [*Prigent et al.*, 2005b]. Higher V emissivities can be observed in regions with a larger presence of sand dunes. This is related to an emission of microwave radiation from deeper soil layers and an associated slight overestimation in the emissivities when deriving them with the infrared skin surface temperature [*Prigent et al.*, 1999]. On the map of the emissivity polarization difference, smooth bare soils have a quasi-specular reflection, producing high polarization emissivity differences around the SSM/I 53° incidence angle. When the terrain gets rougher or vegetation appears (below ~15°N), surface scattering causes the emissivity in horizontal polarization to increase and the polarization difference to decrease. As a consequence, mountainous regions (e.g., Tibesti, Ahaggar, and Hajar) appear with a low polarization difference on the map, whereas flat areas are characterized by high polarization differences. Maps of the 9.3 μm and 10.8 μm yearly averaged emissivities are also presented in Figure 3. At 9.3 μm low emissivity values are related to expected absorption features from silicate minerals and correspond well with the high emissivity values at 37 GHz V associated with the presence of sand dunes. The 10.8 μm emissivity has a limited amplitude of variation but present very clear spatial structures. There is a significant spatial agreement between the low emissivity values at 10.8 μm and the low emissivities at 37 GHz H.

[18] Comparing these maps with the lithology map of Figure 2 allows a qualitative analysis of the emissivities in relation with the outcrops. In general, there is a good correspondence between areas with outcrops composed of siliceous rocks (sand dunes) and the low 9.3 μm and the high 37 GHz V emissivities, though it should be mentioned again that the sensitivity in the microwave emissivities is not related to a sensitivity to the lithology but to a microwave emission from deeper soil layers. The low 10.8 μm and 37 GHz H emissivities also appear in areas where carbonate minerals are present. However, the agreement with the carbonate outcrops does not seem as evident as with the silicates, especially in western Africa. If we zoom over some specific regions, the link between emissivities and lithology is certainly apparent. An example is given in Figure 4, where a cross section over the Arabian Peninsula (~20° latitude) is plotted. The emissivities have been normalized (removing the mean value and dividing by standard deviation) to help the comparison. The changes in the emissivities reasonably follow the changes in the exposed lithology derived from the lithology map of Figure 2.

[19] Histograms of the emissivities for different outcrops in comparison with the histograms of the global emissivities are presented in Figure 5 to highlight the sensitivity of the different emissivities to the silicate and carbonate outcrops. The histograms confirm the observed low emissivity values for carbonates (37 GHz H and 10.8 μm) and silicates (9.3 μm) and show that the lithology types can be well identified. The width of the distributions indicates significant variability within a type, and the overlap with the other histograms confirms that misclassifications can certainly happen. This is anticipated: no perfect matching from a single observation at these large scales can be expected due to the large spatial resolutions, the emissivity errors, the difficulty to interpret the geological maps, or the sensitivity of the observations to other surface parameters. Using multi-observations (i.e., combining microwave and infrared emissivities) could be used to reduce the sensitivity to some of these errors. This will be discussed further in section 3.3.

3.2. Characterization of the Relation Between Lithology and Emissivities

[20] The relation between emissivities and lithology is statistically characterized here. Table 1 shows the mean and standard deviation of the emissivities for the different outcrop types. At 9.3 μm the lowest mean corresponds to the loose siliceous rocks, the next four lower means also have a siliceous component. At 10.8 μm the carbonate rocks have a

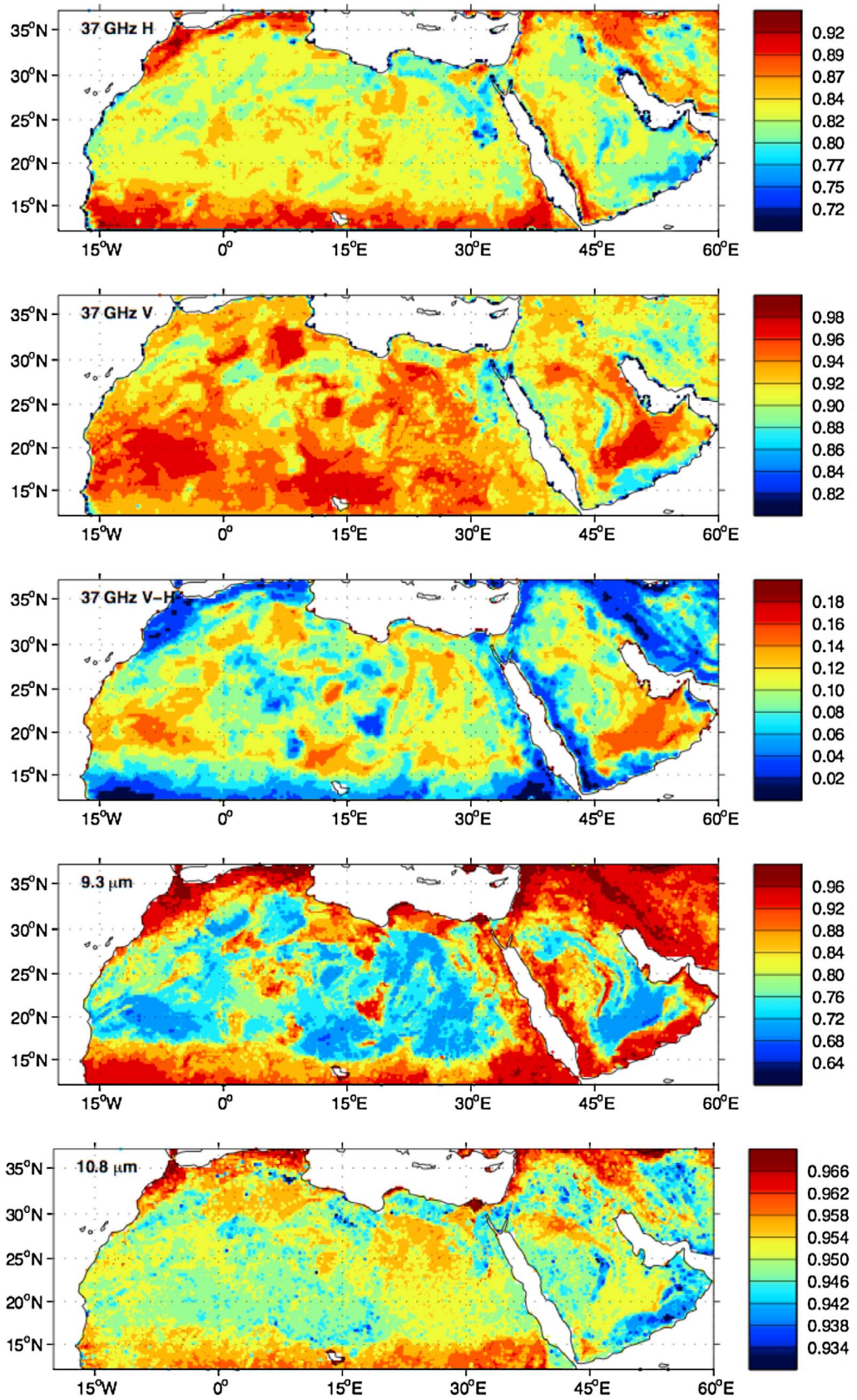

Figure 3. Spatial distributions of yearly averaged emissivities (2003). From top to bottom: (1) 37 GHz H; (2) 37 GHz V; (3) 37 GHz difference (V-H); (4) 9.3 μm; (5) 10.8 μm.

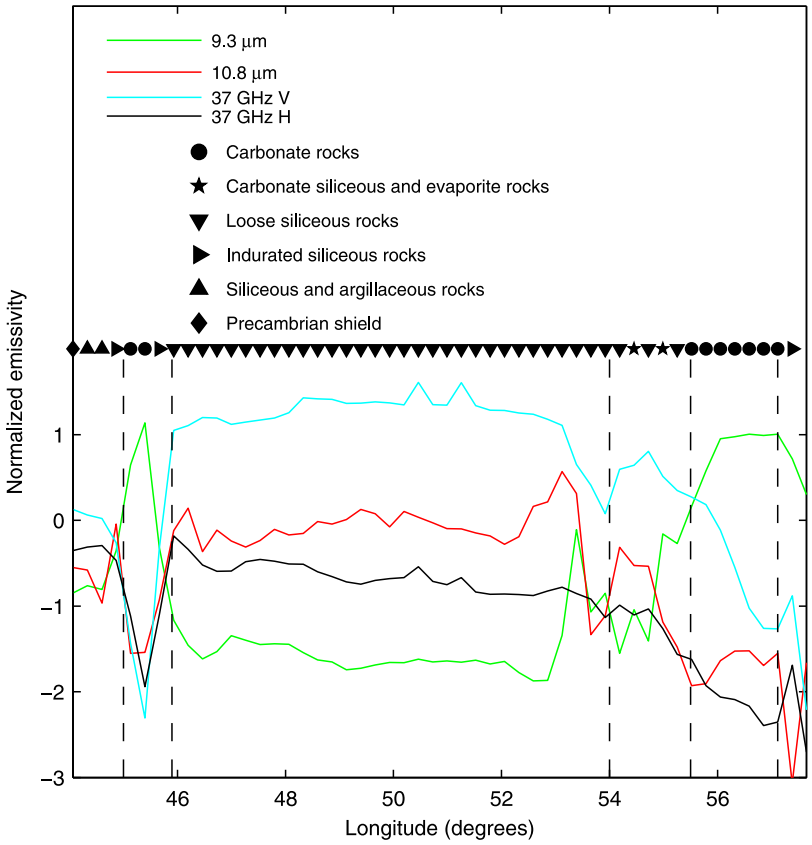

Figure 4. Example of latitudinal cross section over the Arabian Peninsula (20.25°N, 45°E–57°E) for September 2003. The normalized emissivities are plotted at 9.3 μm (green), 10.8 μm (red), 37 GHz V (blue), and 37 GHz H (black). The outcrop for each pixel is given by the different black symbols. The vertical dashed lines indicate the main changes in the lithology.

smaller emissivity than the siliceous sediments, but the differences in the means are much smaller than at 9.3 μm. At 37 GHz V the carbonate rocks have a lower emissivity than the siliceous sediments, and the same is true at 37 GHz H. The regions with evaporites in Tunisia and Algeria have very low emissivities at 37 GHz H, but the signals can also originate from the presence of standing water during a large part of the year in these shatts and sabkhas.

[21] The statistics presented in Table 1 are also used for an analysis of variance (ANOVA). This analysis tries to estimate what part of the observed variability can be assigned to the existence of different outcrops (variance between outcrop type), and what part can be assigned to all other factors contributing to the observed variability (within outcrop type). For each of the four emissivities considered the analysis is carried out by calculating (1) the sum of squares of the deviations of the emissivities around the overall mean (measure of the total variability in the data set), (2) the sum of squares of the deviations of the emissivities for each outcrop type around their respective outcrop means (measure of the variability within different outcrops), and (3) the sum of squares of the deviations of the outcrop mean emissivities from the overall mean (measure of the variability between different outcrops). The sum of squares are then expressed as a variance normalized by their respective degrees of freedom. The variances are given in Table 2. The results show that a large part of the variability in the emissivities (more than 50% for 9.3 μm and ~40% for the other frequencies) can be explained by the lithology. The other parts of the variance are to be attributed to other surface parameters affecting the observations (e.g., roughness), to errors in the geological interpretation mapping, or to uncertainties in the satellite products.

[22] The partitioning of variance is also used to carry out an F test. Under the hypothesis that the lithology is not exerting any control over the emissivities (the null hypothesis), the ratio of the "between" and "within" variances (F ratio) follows an F distribution. Table 2 shows the F ratios for the four emissivities. The ratios are much larger than 1, and the p values obtained assuming that the null hypothesis is true are well below 0.01, allowing to reject the null hypothesis at the 1% significance level. These results suggest that the lithology exerts a notable control on the emissivities. This is consistent with a similar analysis at smaller scales by *Zhou et al.* [2003].

3.3. Potential Mapping of Large-Scale Lithology From the Emissivities

[23] The potential of the emissivities for a large-scale mapping of major lithology features is studied by deriving a lithology classification of the area using the satellite observations. Different supervised and unsupervised classi-

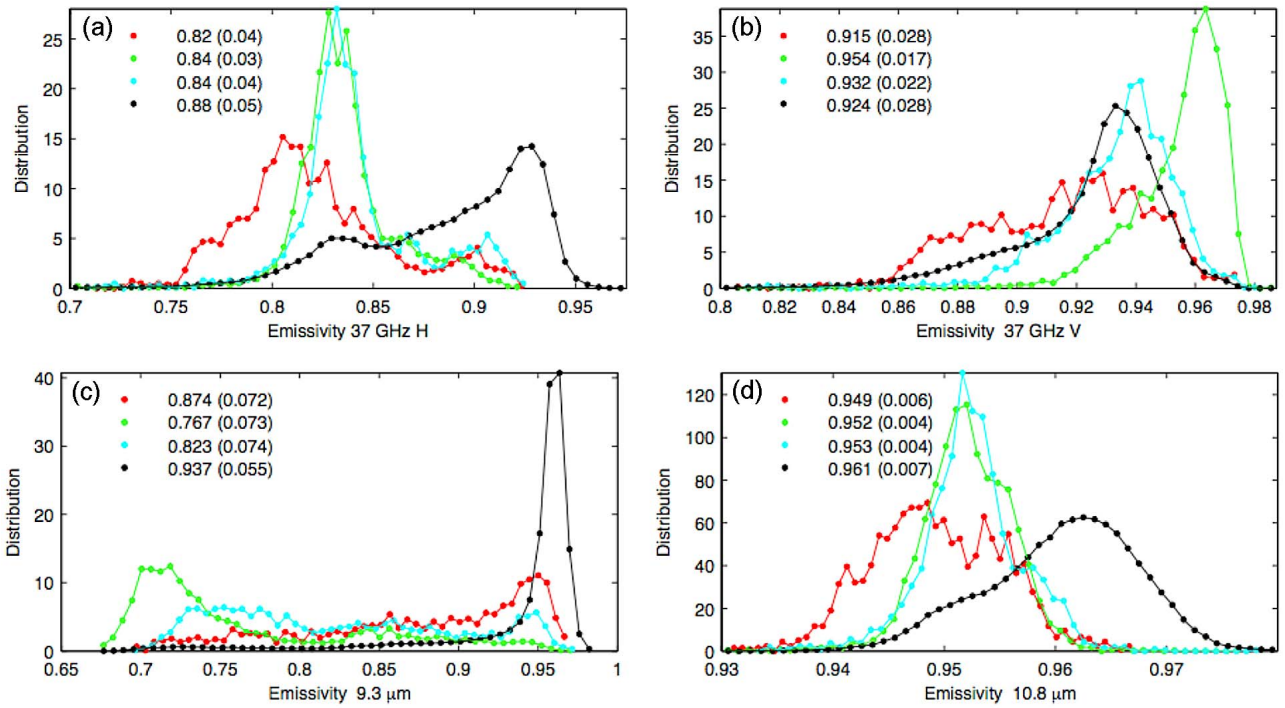

Figure 5. Normalized histograms of the (a) 37 GHz H, (b) 37 GHz V, (c) 9.3 μm, and (d) 10.8 μm emissivities for different outcrops. The histograms for carbonate rocks (red), loose siliceous rocks (green), and indurated siliceous rocks (blue) are displayed over Northern Africa and the Arabian Peninsula. The histograms of the emissivities are also plotted for the whole globe (black). The numbers correspond to the mean emissivity and its standard deviation (in brackets).

fication approaches exist [e.g., *Lu and Weng*, 2007]. The technique adopted here is an unsupervised clustering technique called *K* means [e.g., *Celeux et al.*, 1989]. It partitions n observations into k clusters in which each observation belongs to the cluster with the nearest mean. It is an efficient and fast method when faced with a large classification matrix (as in our case), but the nature of the derived classes can be difficult to interpret, and a postclassification phase is often needed to regroup the initial classes. Supervised classifications (targeting to the same final classes obtained from the unsupervised classification) were also tested (results not presented), with similar results. This suggests that for this specific study the nature of the data is a more limiting factor than the ability of the classification technique.

[24] Previous to the classification, the 9.3 μm, 10.8 μm, and the 37 GHz V and H emissivities are first normalized (zero mean, unity standard deviation, as in Figure 4) and then organized in an emissivity matrix (4 emissivities × n geographical pixels). The *K* means algorithm is then applied over the emissivity matrix. Different numbers of clusters were tested, with satisfactory results obtained with 20 clusters. The geographical patterns of the derived classes can be observed in Figure 6. Some of the classes can be easily related to specific outcrops (e.g., class 9 with loose siliceous rocks and class 4 with carbonate rocks), but for other classes the

Table 1. Mean and Standard Deviation (in Brackets) of Infrared and Microwave Emissivities by Outcrop Type[a,b]

Group	9.3 μm	10.8 μm	37 GHz V	37 GHz H	Pixels
L1	0.845(0.068)	0.948(0.005)	0.914(0.023)	0.806(0.026)	1045
L2	0.824(0.063)	0.950(0.003)	0.925(0.021)	0.823(0.020)	1975
L3	0.741(0.052)	0.951(0.003)	0.955(0.014)	0.829(0.017)	3568
L4	0.790(0.055)	0.951(0.003)	0.931(0.019)	0.828(0.022)	1530
L5	0.782(0.048)	0.950(0.002)	0.931(0.014)	0.825(0.013)	524
L6	0.769(0.058)	0.951(0.003)	0.939(0.017)	0.837(0.015)	1433
L7	0.792(0.053)	0.949(0.002)	0.929(0.016)	0.832(0.015)	812
L8	0.837(0.056)	0.949(0.002)	0.922(0.017)	0.835(0.017)	2034
L9	0.882(0.063)	0.949(0.002)	0.923(0.017)	0.841(0.027)	74
L10	0.919(0.041)	0.947(0.002)	0.909(0.010)	0.846(0.016)	237
L11	0.945(0.002)	0.946(0.002)	0.911(0.009)	0.871(0.019)	6
L12	0.849(0.062)	0.945(0.010)	0.909(0.056)	0.776(0.082)	31

[a]L1, carbonate rocks; L2, carbonate siliceous and evaporite rocks; L3, loose siliceous rocks; L4 indurated siliceous rocks; L5, siliceous argillaceous and evaporite rocks; L6, siliceous argillaceous and carbonate Rocks; L7, siliceous and argillaceous rocks; L8, Precambrian shield; L9, granite; L10, basalt; L11, ophiolite; and L12, evaporite.
[b]The number of pixels for each outcrop type is given in the last column.

Table 2. ANOVA Table for Infrared and Microwave Emissivities[a]

Emissivity	Variance		F
9.3 μm	Between outcrop type	64.12 (50.4)	1544.4
	Within outcrop type	63.18 (49.6)	($p < 0.01$)
10.8 μm	Between outcrop type	0.1857 (38.1)	933.2
	Within outcrop type	0.302 (61.9)	($p < 0.01$)
37 GHz V	Between outcrop type	4.057 (37.7)	918.2
	Within outcrop type	6.720 (62.3)	($p < 0.01$)
37 GHz H	Between outcrop type	7.83 (42.3)	1146.6
	Within outcrop type	10.70 (57.7)	($p < 0.01$)

[a]The variance is given in absolute values and as percentage of the total variance (in brackets). The last column gives the F ratio.

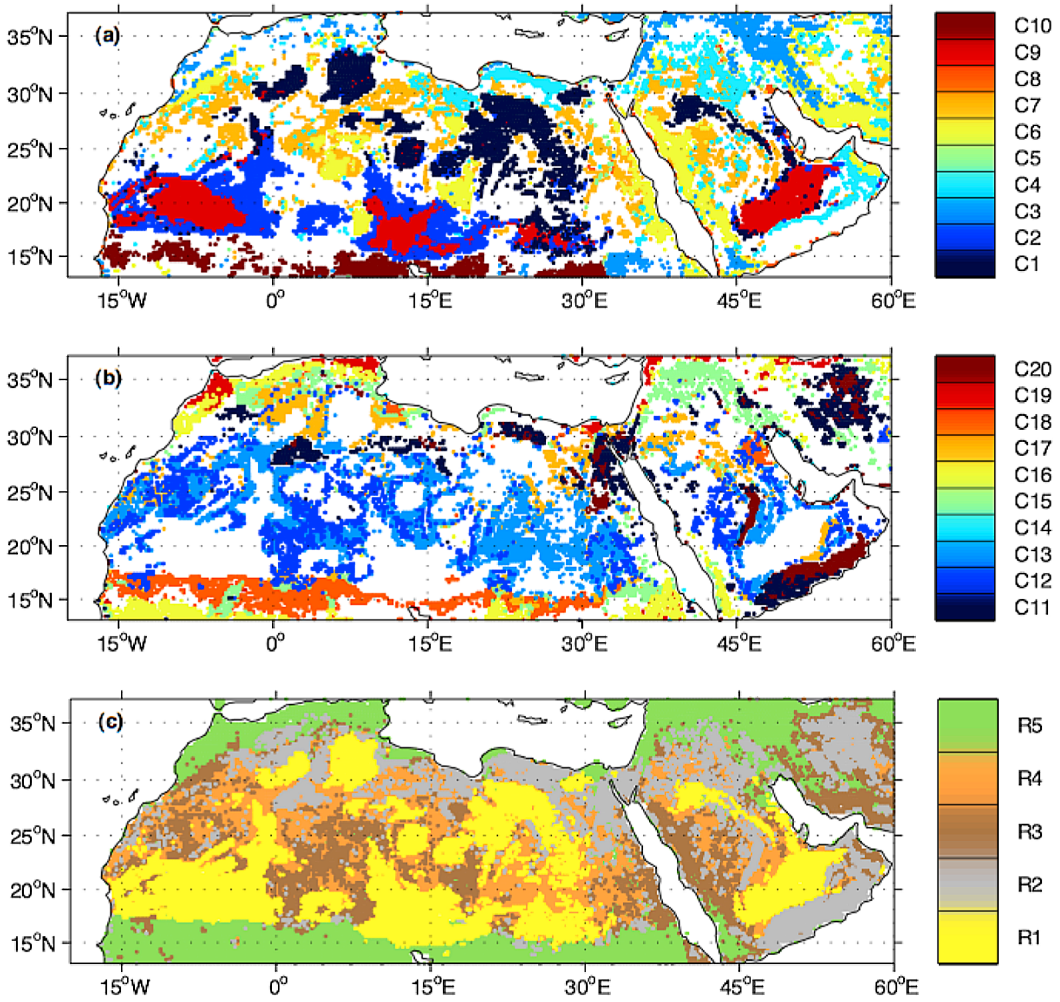

Figure 6. Classes derived from the *K* means nonsupervised classification applied to the annual mean emissivities. (a) The first 10 classes and (b) the remaining 10 classes. (c) The grouping of the original 20 classes into five new classes: (1) siliceous rocks (R1 = C1, C2, C9); (2) carbonate rocks (R2 = C4, C11, C17, C20); (3) metamorphic and igneous rocks (R3 = C6, C12); (4) mixture (R4 = C7, C8, C13, C14); (5) vegetation (R5 = C3, C5, C10, C15, C16, C18, C19). See the text for more details.

interpretation is more difficult. For instance, the classification suggests that we cannot clearly separate the igneous rocks from the metamorphic rocks of the Precambrian shield, and they will be regrouped under a common class. To aid the interpretation of the derived outcrop map, all classes are then regrouped into five new classes in a postclassification phase, where the new classes are established by grouping together the original classes having similar characteristics (as described in the lithology map). The new classes identify the presence of (R1) siliceous rocks, (R2) carbonate rocks, (R3) metamorphic and igneous rocks, (R4) mixture, and (R5) vegetation. The map of the new classes are plotted in Figure 6.

[25] An evaluation of the classification is presented in Table 3. The table lists the number of pixels of a given outcrop type interpreted by the *K* means classification as siliceous rocks (R1), carbonate rocks (R2), and metamorphic and igneous rocks (R3). In general, there is a good correspondence between the *K* means new classes and the outcrops identified in the lithology map. For the carbonate rocks of L1, the largest Pixel Number (PN) is in class R2. L2 is a mixture of carbonate, siliceous, and evaporite rocks (in decreasing order of presence within the mixture), and the PN in R2 > PN in R1 > PN in R3, in accordance with the expected presence of carbonate, siliceous, and metamorphic rocks in the mixture. The loose siliceous rocks of L3 have a very large PN within R1. The indurated siliceous rocks of L4 seem more difficult to classify (PN in R1 > PN in R3 > PN in R2 but not with large differences as for L3). L5, L6, and L7 are mixtures having a large percentage of siliceous rocks, and the largest PN corresponds to R1. The Precambrian shield, granite, and basalt of L8, L9, and L10 have the largest PN in their expected class, that is, R3.

[26] An attempt to derive classification scores follows. For the siliceous rocks, the score is computed as the percentage of pixels in lithology types L3, L4, and L6 classified as R1; for carbonate rocks, the percentage of pixels in L1 and L2 identified as R2; and for metamorphic and igneous rocks, the percentage of pixels in L8, L9, and L10 classified as R3.

Table 3. Number of Pixels From Some of the Original Lithology Types Classified Within the *K* means Regrouped Classes[a]

Lithology	Regrouping		
	R1	R2	R3
L1 Carbonate Rocks	130	588	46
L2 Carbonate Siliceous and Evaporite Rocks	310	637	245
L3 Loose Siliceous Rocks	2592	206	123
L4 Indurated Siliceous Rocks	312	210	229
L5 Siliceous Argillaceous and Evaporite Rocks	99	52	91
L6 Siliceous Argillaceous and Carbonate Rocks	732	96	117
L7 Siliceous and Argillaceous Rocks	172	42	26
L8 Precambrian Shield	121	183	911
L9 Granite	4	8	40
L10 Basalt	1	39	171
Classification Rate	56%	41%	48%

[a]The *K* means classes discussed are as follows: R1, siliceous rocks; R2, carbonate rocks; R3, metamorphic and igneous rocks. Classification rates are given at the bottom of the table, assuming R1 = L3+L4+L6, R2 = L1 +L2, and R3 = L8+L9+L10. Lithology types L11 and L12 have very low pixel counts and are not included. See the text for more details.

The respective classification scores are given at the bottom of Table 3. The figures indicate that approximately one of two pixels is well classified. Taking into account the limitations in the satellite observations and in the lithology mapping, this result is encouraging. The spatial resolution of the satellite data, their processing errors, and the sensitivity of the observations to other surface parameters hamper a more accurate mapping. At these large scales, no official lithology map exists and the methodology we adopted to derive one is not perfect. Uncertainties come from the ambiguities in the age of the geological formations, the precise composition of the sedimentary rocks, the geological structure in the lithostratigraphic columns, the fact that the lithostratigraphic information has been geographically extrapolated, and the necessary spatial integration of the lithology information into a pixel of a given area. Moreover, the geological structures are not perfectly mapped at these large scales. As an example, two sections of the USGS geological map (used to derive the lithology map in section 2.3) are plotted in Figure 7 together with the corresponding sections from a different map (the "Bureau de Recherches Géologiques et Minières" (BRGM) SIG Afrique geological map). The regions correspond to Northwest and Northeast Africa. Relatively large differences in the mapped geological structures can be found in some regions. For instance, less geological details can be observed in the BRGM map over Northeast Africa between Egypt and Libya (large light yellow region), compared with the USGS map. These features are also well captured by our satellite-derived map (Figure 6) but are absent on the BRGM map that is devoted to mineral exploration and much more focused on ore-rich shields.

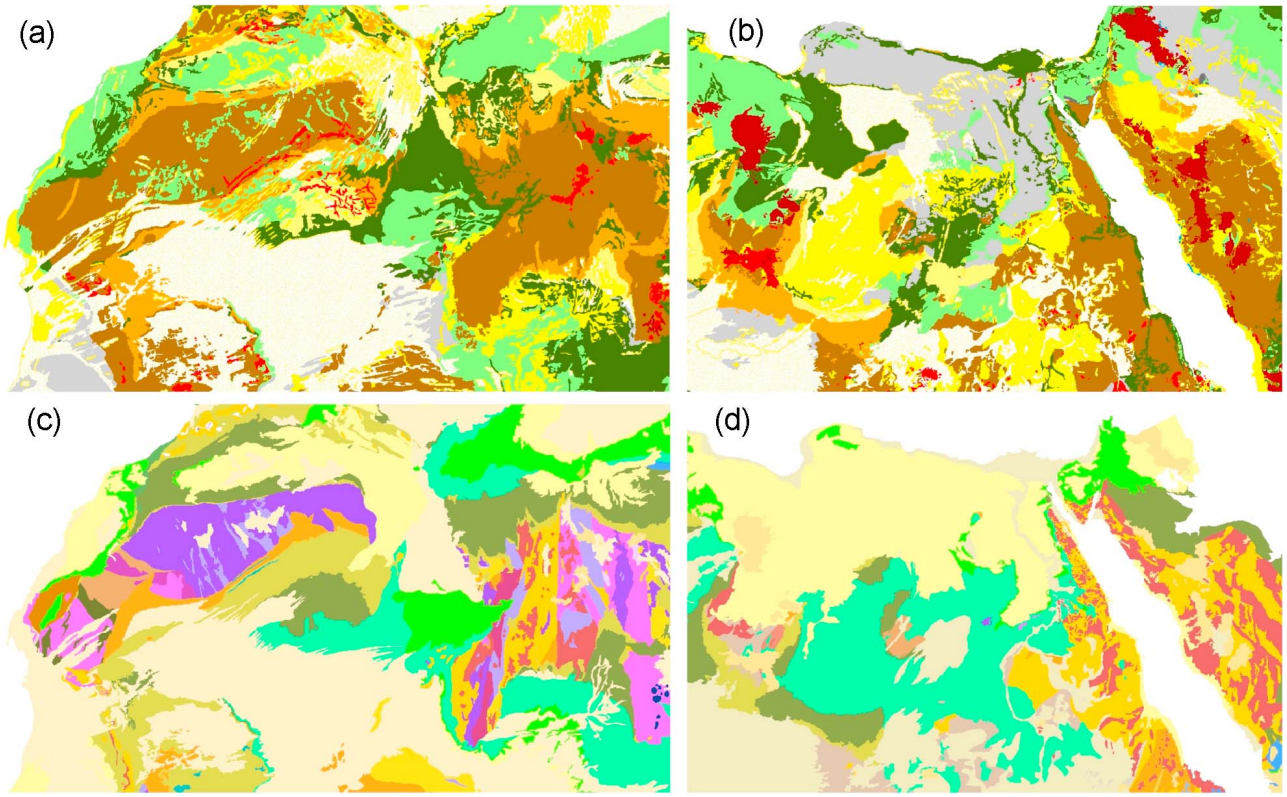

Figure 7. Example of large-scale available geological maps. (a and c) Regions from the USGS map; (b and d) the same regions from the BRGM map. Each map uses a different color map to represent the different geological periods (legends not given). Northwest Africa is presented in Figures 7a and 7c and Northeast Africa in Figures 7b and 7d. See the text for more details.

These structures are actually related to the carbonate outcrops that are already visible on the raw emissivity map at 37 GHz H (emissivity values of ~0.7 at the top panel in Figure 3). In the Precambrian shields over Northwest Africa, it is now the USGS map (large dark brown areas) that shows much less details, compared with the BRGM map. These differences possibly reflect the main objectives of the two geological maps. The satellite systematic observations with global coverage provide a consistent and objective analysis of the large areas, regardless of specific local studies or particular interest for a given region.

[27] Taking into account the uncertainties, both in the satellite observations and in the lithology, this exercise shows that a combined exploitation of the infrared and microwave emissivities can help characterize arid regions, as a complement to more traditional methods and observations at other wavelengths. Note that the low spatial resolution of the present microwave observations from space limits their potential to large-scale applications. The combined exploitation is particularly useful at large scales, where the downgraded spatial resolution (compared with only using the infrared emissivities) is not a drawback. In particular, we argue that in order to better specify emissivities in GCMs and NWP schemes the satellite-derived data is a direct and efficient way to specify the surface lithology and to complement the derivation of relevant surface properties from existing geological maps. In addition, this technique can also be very valuable for the mapping of inaccessible regions, e.g., for planetology exploration.

4. Conclusions

[28] Infrared and microwave emissivities have been previously calculated over the globe from satellite observations, to estimate the longwave radiative budget of the planet in GCM or to facilitate the assimilation of surface-sensitive satellite observations over land in NWP models. This study examines the relationship between these emissivities and the soil lithography, over the deserts in Northern Africa and in the Arabian Peninsula, at large scales. For this purpose, a lithology map of the area has been derived by merging information from different geological maps and lithostratigraphic columns. Infrared and microwave emissivities have large spatial variability, much more than is often assumed in GCM or in NWP models, that are related with surface properties, especially the lithology. This study showed the consistency of the two emissivity data sets, giving confidence in each one, at large scale, and proves that lithology information is a prerequisite for emissivity modeling, not only in the infrared domain but also in the microwaves, for GCM and NWP applications. Similar geological information is also necessary for the interpretation of 1.4 GHz measurements from the Soil Moisture and Ocean Salinity mission, launched in November 2009.

[29] Satellite observations at high spatial resolution are already used for geological applications at different wavelengths. The emissivities and reflectances derived from measurements in the short wave infrared provide information on the nature of the minerals in arid regions. For instance, the Advanced Spaceborne Thermal Emission and Reflection Radiometer (ASTER) on board TERRA gives high-resolution land surface temperature, emissivity, and reflectance from which desert surface mapping can be derived [e.g., *Amer et al.*, 2009]. At much longer wavelengths, microwave radar techniques are used for terrestrial and planetological applications to explore the surface and subsurface in arid areas [e.g., *Grandjean et al.*, 2006; *Lorenz et al.*, 2008]. Synthetic Aperture Radar at high resolution, eventually used in interferometry modes, are adopted to analyze morphological changes, such as volcanic activity or landslides [e.g., *Sachpazi et al.*, 2002; *Colesanti and Wasowski*, 2006]. This study suggests that passive microwave observations can also have potential for geological application at large scales to complement the other satellite observations. Measurements of the dielectric properties of rocks and sands are underway, between 1 and 600 GHz, to consolidate these findings and provide an explanation for the large permittivity measured in carbonated rocks.

[30] **Acknowledgments.** We acknowledge Suzanne Seemann and Eva Borbas from the University of Wisconsin for kindly providing their emissivity data set and making valuable comments to improve this manuscript. The Jet Propulsion Laboratory from the California Institute of Technology is acknowledged for making accessible the ASTER Spectral Library. We are grateful to Laurie Barrier from the Institut de Physique du Globe de Paris for her extensive advice for the compilation of the lithology map. The Service des Ressources Minérales from the Bureau des Ressources Géologiques et Minières is acknowledged for kindly providing the digital version of the 1/10M SIG Afrique geological map. The United States Geological Survey is also acknowledged by allowing access to the digital version of the Bedrock Geology of the Arabian Peninsula and Selected Adjacent Areas map.

References

Aires, F., C. Prigent, W. Rossow, and M. Rothstein (2001), A new neural network approach including first-guess for retrieval of atmospheric water vapor, cloud liquid water path, surface temperature and emissivities over land from satellite microwave observations, *J. Geophys. Res.*, *106*(D14), 14,887–14,907.

Allison, L. (1977), *Geological Applications of Nimbus Radiation Data in the Middle East*, *Tech. Rep.*, NASA Technical Note, TND-8469.

Amer, R., T. Kusky, and A. Ghulam (2009), Lithological mapping in the Central Eastern Desert of Egypt using ASTER data, *J. Afr. Earth Sci.*, doi:10.1016/j.jafrearsci.2009.06.004.

Baldridge, A., S. Hook, C. Grove, and G. Rivera (2009), The ASTER spectral library version 2.0, *Remote Sens. Environ.*, *113*(4), 711–715.

Campbell, M. J., and J. Ulrichs (1969), Electrical properties of rocks and their significance for lunar radar observations, *J. Geophys. Res.*, *74*(25), 5867–5881.

Celeux, G., E. Diday, G. Govaert, Y. Lechevallier, and H. Ralambondrainy (1989), *Classification automatique des données*, Dunod, Paris.

Chédin, A., E. Péquignot, S. Serrar, and N. Scott (2004), Simultaneous determination of continental surface emissivity and temperature from NOAA 10/HIRS observations: Analysis of their seasonal variations, *J. Geophys. Res.*, *109*, D20110, doi:10.1029/2004JD004886.

Colesanti, C., and J. Wasowski (2006), Investigating landslides with space-borne Synthetic Aperture Radar (SAR) interferometry, *Eng. Geol. Amsterdam*, *88*(3–4), 173–199.

Dai, Y., et al. (2003), The Common Land Model (CLM) version 1.0, *Bull. Am. Meteorol. Soc.*, *84*(8), 1013–1023.

Grandjean, G., P. Paillou, N. Baghdadi, E. Heggy, T. August, and Y. Lasne (2006), Surface and subsurface structural mapping using low frequency radar: A synthesis of the Mauritanian and Egyptian experiments, *J. Afr. Earth Sci.*, *44*(2), 220–228.

Hulley, J., and S. Hook (2009), The North American ASTER Land Surface Emissivity Database (NAALSED) Version 2.0, *Remote Sens. Environ.*, *113*, 1967–1975.

Karbou, F., C. Prigent, L. Eymard, and J. Pardo (2005), Microwave land emissivity calculations using AMSU measurements, *IEEE Trans. Geosci. Remote Sens.*, *43*(5), 948–959.

Kinter, J. L., J. Shukla, L. Marxand, and E. K. Schneider (1988), A simulation of the winter and summer circulations with the NMC global spectral model, *J. Atmos. Sci.*, *45*, 2486–2522.

Lebron, I., D. A. Robinson, S. Goldberg, and S. M. Lesch (2004), The dielectric permittivity of calcite and arid zone soils with carbonate minerals, *Soil Sci. Soc. Am.*, *68*, 1549–1559.

Li, J., J. Li, E. Weize, and D. K. Zhou (2007), Physical retrieval of surface emissivity spectrum from hyperspectral infrared radiances, *Geophys. Res. Lett.*, *34*, L16812, doi:10.1029/2007GL030543.

Lorenz, R., et al. (2008), Fluvial channels on Titan: Initial Cassini RADAR observations, *Planet. Space Sci.*, *56*(8), 1132–1144.

Lu, D., and Q. Weng (2007), A survey of image classification methods and techniques for improving classification performance, *Int. J. Remote Sens.*, *28*(5), 823–870.

Nelson, S. O., D. P. Lindroth, and R. L. Blake (1989), Dielectric properties of selected minerals at 1 to 22 GHz, *Geophysics*, *54*, 1344–1349.

Ogawa, K., T. Schmugge, F. Jacob, and A. French (2003), Estimation of land surface window (8–12 micron) emissivity from multi-spectral thermal infrared remote sensing: A case study in a part of Sahara Desert, *Geophys. Res. Lett.*, *30*(2), 1067, doi:10.1029/2002GL016354.

Prigent, C., W. B. Rossow, and E. Mathews (1997), Microwave land surface emissivities estimated from SSM/I observations, *J. Geophys. Res.*, *102*(D18), 21,867–21,890.

Prigent, C., W. B. Rossow, and E. Mathews (1999), Microwave radiometric signatures over different surface types in deserts, *J. Geophys. Res.*, *104*(D10), 12,147–12,158.

Prigent, C., F. Chevallier, F. Karbou, P. Bauer, and G. Kelly (2005a), AMSU-A land surface emissivity estimation for numerical weather prediction assimilation schemes, *J. Appl. Meteorol*, *44*, 416–426.

Prigent, C., J.-M. Munier, B. Thomas, and G. Ruffié (2005b), Microwave signatures over carbonated platforms in arid areas: Potential geological applications of passive microwave observations?, *Geophys. Res. Lett.*, *32*, L23405, doi:10.1029/2005GL024691.

Prigent, C., F. Aires, and W. Rossow (2006), Land surface microwave emissivities over the globe for a decade, *Bull. Am. Meteorol. Soc.*, *87*, 1573–1584.

Rossow, W., and R. Schiffer (1999), Advances in understanding clouds from ISCCP, *Bull. Am. Meteorol. Soc.*, *80*(11), 2261–2287.

Sachpazi, M., et al. (2002), Seismological and SAR signature of unrest at Nisyros caldera, Greece, *J. Volcanol. Geotherm. Res.*, *116*, 19–33.

Salisbury, J. W., A. Wald, and D. M. D'Aria (1994), Thermal-infrared remote sensing and Kirchoff's law 1. Laboratory measurements, *J. Geophys. Res.*, *99*, 11,897–11,911.

Seemann, S. W., E. E. Borbas, R. O. Knuteson, G. R. Stephenson, and H.-L. Huang (2008), Development of a global infrared surface emissivity database for application to clear sky retrievals from multispectral satellite radiance measurements, *J. Appl. Meteorol. Climatol.*, *47*, 108–123.

Thomas, B. (2006), Microwave dielectric properties of minerals and rocks, in *Thermal Microwave Radiation: Applications for Remote Sensing*, edited by A. B. C. Matzler, P. W. Rosenkranz and J. Wigneron, IEEE Electromagnetic Waves Series, London, UK.

Wan, Z. (2008), New refinements and validation of the MODIS Land-Surface Temperature/Emissivity products, *Remote Sens. Environ.*, *112*(1), doi:10.1016/j.rse.2006.06.026.

Wan, Z., and Z.-L. Li (1997), A Physics-based algorithm for retrieving land-surface emissivity and temperature from EOS/MODIS data, *IEEE Trans. Geosci. Remote Sens.*, *35*, 980–996.

Weng, F., and Q. Liu (2003), Satellite data assimilation in numerical weather prediction models, Part I: Forward radiative transfer and Jocobian modeling in cloudy atmospheres, *J. Atmos. Sci.*, *60*, 2633–2646.

Zeng, X., M. Shaikh, Y. Dai, R. E. Dickinson, and R. B. Myneni (2002), Coupling of the common land model to the NCAR community climate model, *J. Clim.*, *14*, 1832–1854.

Zhou, L., R. E. Dickinson, K. Ogawa, Y. Tian, M. Jin, T. Schmugge, and E. Tsetsinskaya (2003), Relations between albedos and emisisvities from MODIS and ASTER data over North African desert, *Geophys. Res. Lett.*, *30*(20), 2026, doi:10.1029/2003GL018069.

J. Catherinot, C. Jiménez, and C. Prigent, Laboratoire d'Etudes du Rayonnement et de la Matière en Astrophysique, CNRS, Observatoire de Paris, 61, avenue de l'Observatoire, F-75014 Paris, France.

J. Roger, Bureau des Ressources Géologiques et Minières, 3 avenue Claude-Guillemin, BP 36009, 45060 Orléans Cedex 2, France.